

Topological Dislocation Response in Elementary Semiconductors

Yuteng Zhou,¹ Alexandre Chaduteau,¹ and Frank Schindler¹

¹*Blackett Laboratory, Imperial College London, London SW7 2AZ, United Kingdom*

We study elementary semiconductors and insulators that are symmetric under spatial inversion: silicon, diamond, germanium, and black phosphorene. These materials are ideal candidates for realizing obstructed atomic insulators, which differ from trivial atomic insulators by a quantized spatial shift of their electronic Wannier centers with respect to the atomic lattice. We use symmetry indicator invariants that allow the prediction of non-trivial responses to crystal dislocations in these materials. We find that edge dislocations generically exhibit a non-trivial response, while screw dislocations always display a trivial response. With the aid of numerical simulations of realistic tight-binding models, we confirm the presence of mid-gap polarization bands localized along dislocations in silicon, diamond, and germanium.

Introduction— The theory of non-interacting topological insulators (TIs) [1–3] can be considered quite mature. TIs can host edge states that are robust under perturbations; their presence is diagnosed by bulk topological invariants. Besides edges, crystals will inevitably host imperfections such as crystal defects [4] that alter the local geometry of the lattice. Refs. 5–21 have defined topological invariants to diagnose the presence of robust bound states localized at such defects. In particular it was found that dislocations – stable line defects in three-dimensional (3D) crystals that disrupt translational symmetry only locally – can host topologically protected one-dimensional (1D) “first-order” gapless helical modes [5] and zero-dimensional (0D) “higher-order” end states [9], which are protected by spinful time reversal (\mathcal{T}) and inversion (\mathcal{I}) symmetry, respectively. This response has been discussed for integer Burgers vector dislocations in insulators such as BiSb [5], PbTe monolayers and SnTe [9], elementary bismuth [22], as well as in acoustic and photonic systems [23, 24].

We here apply this theory to some of the most widely studied \mathcal{I} and \mathcal{T} -symmetric elementary semiconductors [25]: 3D silicon, diamond, germanium, and two-dimensional (2D) black phosphorene (BP). These materials are obstructed atomic insulators (OAI) [26–49] whose symmetric and exponentially-localized electronic Wannier functions are not centered at atomic sites [50]. We use topological invariants inspired by Ref. 9 to diagnose the dislocation response of 2D BP and 3D silicon, diamond and germanium. Via realistic tight-binding models, we confirm that when introducing edge dislocations, these semiconductors exhibit floating bands localized along the dislocation inside the gap of the energy spectrum. We call them polarization bands as they arise from the bulk polarization, similar to the end states of the Su-Schrieffer-Heeger (SSH) chain [51, 52]. Since it is impossible to remove the degeneracy between polarization bands associated with spatially separated (and \mathcal{I} -related) dislocations without breaking \mathcal{I} and \mathcal{T} symmetry, a filling anomaly occurs and furnishes a topologically protected defect response of the OAI phase [53, 54]. We also prove that screw dislocations cannot bind polarization bands.

Topological invariants for dislocation response— In 2D TIs with \mathcal{I} and \mathcal{T} symmetry, the \mathbb{Z}_2 Fu-Kane invariant [55, 56] diagnoses the presence of an odd number of robust pairs of helical edge states. This notion was extended to 3D \mathcal{I} - and \mathcal{T} -symmetric TIs which now have four \mathbb{Z}_2 invariants $(\nu_0, \nu_1, \nu_2, \nu_3)$ implying the presence of topological surface states. Here $\nu_i = 0, 1$, $i = 1, 2, 3$, are called weak invariants, which may be packaged into a vector $\mathbf{M}_\nu = (\nu_1 \mathbf{b}_1 + \nu_2 \mathbf{b}_2 + \nu_3 \mathbf{b}_3)/2$, where $(\mathbf{b}_1, \mathbf{b}_2, \mathbf{b}_3)$ are reciprocal basis lattice vectors [5, 9]. These invariants rely on translational symmetry. The other “strong” topological invariant $\nu_0 = 0, 1$ in principle does not require translational invariance (though it may be easier to calculate in momentum space) and describes surface states that are robust against disorder. A 3D weak TI – which only has the weak invariants non-vanishing – can be adiabatically related to a disconnected stack of 2D TIs along the real-space direction dual to \mathbf{M}_ν .

For OAIs, all four Fu-Kane invariants are trivial by the assumption that we can find exponentially localized Wannier states, so that we do not expect gapless surfaces. Nevertheless, when introducing dislocations that cut through the Wannier centers, OAIs can host polarization-induced bound states [9]. More formally, a bulk-defect correspondence can be formalized via the notion of filling anomaly [53]: at neutral filling, dislocation bound states that are related by \mathcal{I} symmetry are only half-filled on average. The resulting ground state degeneracy can only be lifted by breaking \mathcal{I} symmetry or closing the bulk gap. In particular, it remains even when the dislocation bound states are pushed out of the gap and hybridize with the bulk states, thus serving as a robust dislocation response diagnosing the OAI phase absent fine tuning. In ideal situations, moreover, the defect-localized states form a floating band *inside* the bulk gap. Though this is not guaranteed to happen, we will show that this case is realized in 3D semiconductors.

We now construct topological invariants that predict dislocation-induced filling anomalies in OAIs [9]. Consider a generic d -dimensional \mathcal{I} -symmetric (and optionally \mathcal{T} -symmetric) crystal. We label basis lattice vectors by \mathbf{a}_i , $i \in \{1, \dots, d\}$, and reciprocal basis lattice

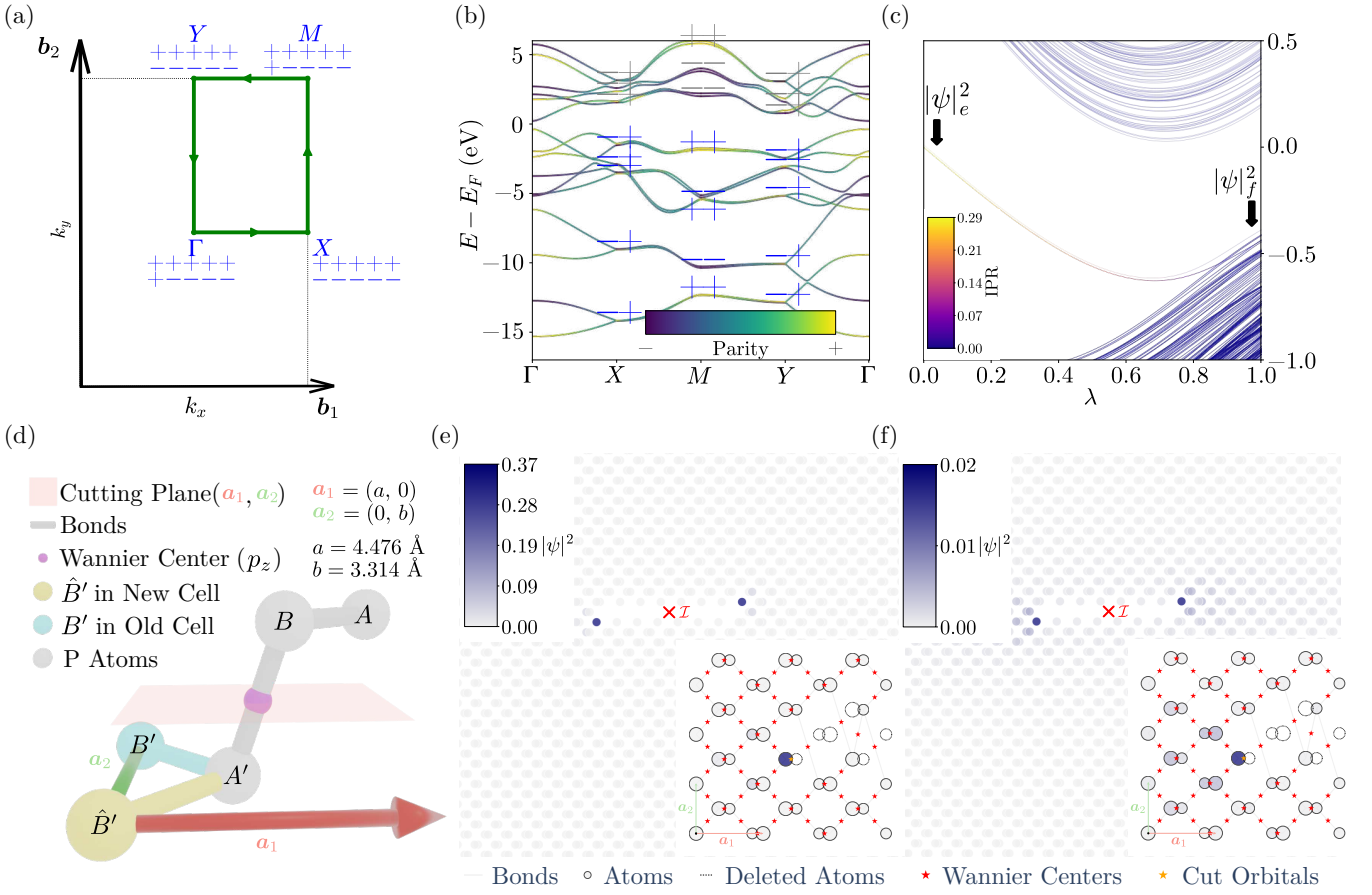


FIG. 1. Dislocation response of black phosphorene (BP). (a) Brillouin zone of BP, showing time-reversal invariant momentum (TRIM) [9] points and their occupied inversion eigenvalues. (b) Band structure along the path shown in (a), with associated inversion eigenvalues at TRIMs. (c) Spectrum in presence of a pair of \mathcal{I} -related dislocations, plotted against the interpolation parameter λ [see Eq. (7)]. Two polarization bands appear inside the gap. One of them is slightly shifted to aid visualization. We color-code their IPR, which is maximal at $\lambda = 0$ (90° model) and minimal at $\lambda = 1$ (realistic model) [see Eq. (7)]. Simulations are performed on a lattice of 30×30 unit cells spanned by \mathbf{a}_1 and \mathbf{a}_2 . The dislocation is introduced by cutting the lattice (keeping unit cells intact), removing 7 unit cells, and gluing back together. (d) Unit cell of BP, consisting of 4 phosphorus atoms, each of which has 5 valence electrons. The commonly used unit cell consists of the gray and blue atoms (A , B , A' and B'). By contrast, the unit cell we use consists of the gray yellow atoms (A , B , A' and \hat{B}'). This choice ensures that the edge dislocation preserves \mathcal{I} symmetry. The positions of these atoms in terms of fractional lattice vectors are: $\tau_A = [(1/2 - u)a, b/2, c]$, $\tau_B = (ua, 0, c)$, $\tau_{A'} = -\tau_B$, $\tau_{B'} = -\tau_A + \mathbf{a}_2$ and $\tau_{\hat{B}'} = -\tau_A$, where $u = 0.08056$ and $c = 1.0654 \text{ \AA}$ [57]. The pink sphere represents the Wannier center induced by the p_z orbital; the red plane, which in our simulation connects the two \mathcal{I} -related edge dislocations, cuts through it. (e),(f) Real-space wavefunction density $|\psi|^2$ plots of polarization states for $\lambda = 0$ and $\lambda = 1$, respectively, with inversion center shown in red.

vectors by \mathbf{b}_i . There are 2^d time-reversal invariant momentum (TRIM) points in the d -dimensional Brillouin zone (BZ). Each point is labeled by $\alpha = (n_1, \dots, n_d)$, a tuple of d numbers $n_i = 0, 1$ so that its momentum reads $\mathbf{k}_\alpha = \sum_{i=1}^d n_i \mathbf{b}_i / 2$. These momenta \mathbf{k}_α satisfy $\mathbf{k}_\alpha = -\mathbf{k}_\alpha \text{ mod } \mathbf{G}$, where \mathbf{G} is any linear integer combination of the \mathbf{b}_i . We define the index

$$\delta_\alpha = \prod_{m=1}^N \xi_m(\mathbf{k}_\alpha) \xi_m^A(\mathbf{k}_\alpha), \quad (1)$$

where $\xi_m(\mathbf{k}_\alpha)$ and $\xi_m^A(\mathbf{k}_\alpha)$ are, respectively, the inversion eigenvalues of the occupied bands $m = 1 \dots N$ and for a

reference unobstructed atomic limit [9], at the TRIM \mathbf{k}_α .

In 2D, following notation from Ref. [9], we define a two-component weak SSH invariant $M_\nu^{\text{SSH}} = (\nu_1^{\text{SSH}} \mathbf{b}_1 + \nu_2^{\text{SSH}} \mathbf{b}_2) / 2$ via

$$\nu_i^{\text{SSH}} = \frac{1}{2} \left[1 - \prod_{\alpha} (\delta_\alpha)^{\mathbf{k}_\alpha \cdot \mathbf{a}_i / \pi} \right], \quad i \in \{1, 2\}, \quad (2)$$

where α runs over all TRIM points in the first BZ. Intuitively, ν_i^{SSH} is nonzero and equal to 1 when the 1D Bloch Hamiltonian defined on the momentum space line $\mathbf{k} \cdot \mathbf{a}_i = \pi \text{ mod } 2\pi$ has a non-vanishing (time-reversal) polarization [58, 59], as exemplified in a SSH chain [60]. If

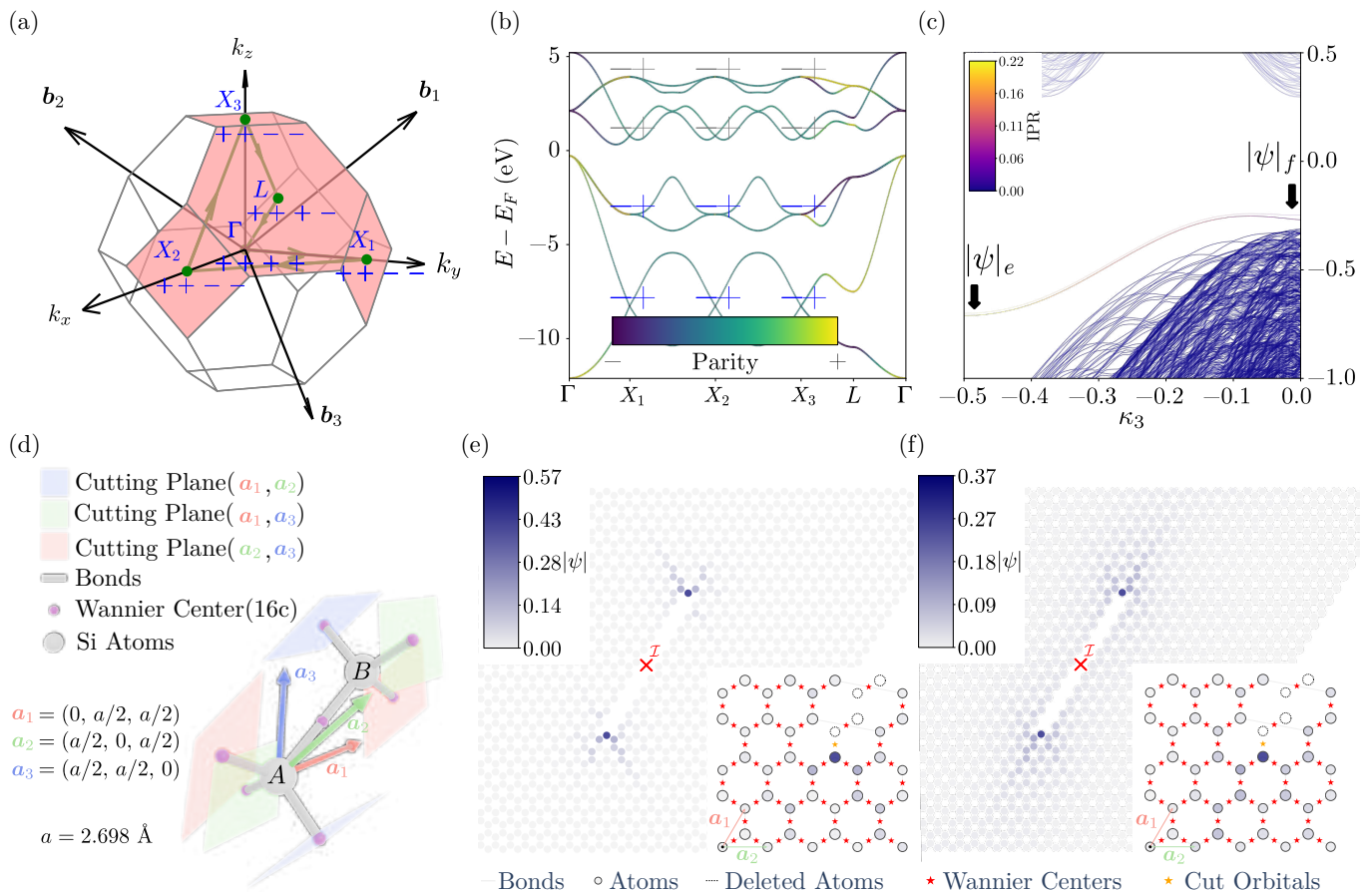


FIG. 2. Edge dislocation response of 3D silicon. (a) Brillouin zone of silicon, showing time-reversal invariant momentum (TRIM) [9] points and their occupied inversion eigenvalues. (b) Band structure along the path shown in (a), with associated inversion eigenvalues at TRIMs. (c) Band structure with a pair of \mathcal{I} -related dislocations present, plotted against the only remaining momentum quantum number $\kappa_3 = (\mathbf{k} \cdot \mathbf{a}_3)/2\pi$. The band structure for positive κ_3 can be obtained by reflection along the $\kappa_3 = 0$ axis because of \mathcal{T} symmetry. Simulations are performed on a lattice of 30×30 unit cells spanned by \mathbf{a}_1 and \mathbf{a}_2 with 100 sample points for momentum κ_3 . The dislocation is introduced by cutting the 3D material along a plane (keeping unit cells intact), removing 10 unit cells, and then gluing the lattice back together [9]. We enforce periodic boundary conditions in all three directions. (d) Real-space unit cell geometry, common to all three 3D semiconductors that we study. There are two silicon atoms in a unit cell, with positions $\tau_A = (0, 0, 0)$ and $\tau_B = \frac{1}{4}(1, 1, 1)$ in fractional lattice vectors. (e),(f): Real-space wavefunction $|\psi|$ plots for polarization states at $\kappa_3 = -1/2$ and $\kappa_3 = 0$, respectively, with inversion center shown in red. We plot the absolute value of the amplitude instead of the density here for a more detailed visualization.

we consider a pair of dislocations related by \mathcal{I} -symmetry, filling-anomalous bound states will be present when the dislocation Burgers vector \mathbf{B} satisfies [5, 9]

$$\mathbf{B} \cdot \mathbf{M}_\nu^{\text{SSH}} \bmod 2\pi = \pi. \quad (3)$$

We will use this condition for BP, a 2D semiconductor.

Let us move on to 3D. Edge dislocations break translational symmetry in two directions out of three, leaving only one good quantum number, a reduced momentum $\kappa_{\parallel} = \mathbf{k} \cdot \mathbf{T}/2\pi$ along the dislocation *line vector* \mathbf{T} . For edge dislocations, \mathbf{T} is a different lattice vector than the Burgers vector \mathbf{B} . We can therefore view κ_{\parallel} as an external pumping parameter between two \mathcal{I} -symmetric 2D Hamiltonians, each in presence of a dislocation, that are defined at $\kappa_{\parallel} = 0$ and $\kappa_{\parallel} = 1/2$. OAI must have identi-

cal weak SSH invariants $\mathbf{M}_\nu^{\text{SSH}}$ for these two 2D Hamiltonians because their 3D weak index \mathbf{M}_ν vanishes. As a result, they cannot host the gapless dislocation states of Refs. [5, 61], but they can still stabilize filling-anomalous polarization bands at edge dislocations if $\mathbf{M}_\nu^{\text{SSH}}$ defined at $\kappa_{\parallel} = 0, 1/2$ satisfies Eq. (3). Conversely, screw dislocations have their line vector \mathbf{T} parallel to the Burgers vector \mathbf{B} . At $\kappa_{\parallel} = 0$, the 2D Hamiltonians with or without the screw dislocation are identical [9] and therefore dislocation-bound polarization bands cannot exist.

We now formalize these observations for general dislocations. Define the 3D weak SSH invariants as a matrix

$$\hat{M}_\nu^{\text{SSH}} = \frac{1}{4\pi} \sum_{i,j=1}^3 \nu_{ij}^{\text{SSH}} \mathbf{b}_i \otimes \mathbf{b}_j, \quad (4)$$

where \otimes denotes the outer product and

$$\nu_{ij}^{\text{SSH}} = \frac{1}{2} \left[1 - \prod_{\alpha} \delta_{\alpha}^{(\mathbf{k}_{\alpha} \cdot \mathbf{a}_i)(\mathbf{k}_{\alpha} \cdot \mathbf{a}_j)/\pi^2} \right]. \quad (5)$$

Here, α runs over all 8 TRIM points in the 3D BZ. For any \mathcal{I} -symmetric pair of dislocations (edge, screw, or mixed) with Burgers vector \mathbf{B} and line vector \mathbf{T} , filling-anomalous polarization bands that disperse with a reduced momentum quantum number κ_{\parallel} along \mathbf{T} will be present in a 3D OAI when

$$\mathbf{B} \cdot (\hat{M}_{\nu}^{\text{SSH}} \cdot \mathbf{T}) = \pi \text{ mod } 2\pi. \quad (6)$$

Eq. (5) implies that $\nu_{i,j}^{\text{SSH}} = \nu_{j,i}^{\text{SSH}}$, meaning the dislocation response is invariant under an exchange of \mathbf{B} and \mathbf{T} . The trivial response for screw dislocations is reflected in the fact that $\nu_{i,i}^{\text{SSH}}$ reduces to the weak invariant ν_i , which is always zero for OAIs.

Dislocation response of black phosphorene— We first consider BP, a 2D material whose puckered honeycomb geometry is depicted in Fig. 1(d), which also defines the lattice basis vectors $\mathbf{a}_1, \mathbf{a}_2$ and associated lattice constants a, b . The BP Hamiltonian we use interpolates between two models [62] with a parameter $0 \leq \lambda \leq 1$. The first model $H_{90^{\circ}}(\mathbf{k})$ assumes a 90° angle between bonds in the puckered structure; it has a chiral symmetry which pins dislocation bound states at zero energy. The second model is a realistic model $H_{\text{black}}(\mathbf{k})$ of BP, which does not have this additional symmetry. Following Ref. 62, we have

$$H_{\lambda}(\mathbf{k}) = (1 - \lambda)H_{90^{\circ}}(\mathbf{k}) + \lambda H_{\text{black}}(\mathbf{k}). \quad (7)$$

Using either model, we obtain the same inversion eigenvalues shown in Figs. 1(a) and (b), which result in $(\nu_1^{\text{SSH}}, \nu_2^{\text{SSH}}) = (1, 1)$ [63], and the bulk gap does not close as we tune $\lambda = 0 \rightarrow 1$. Therefore we obtain $\mathbf{M}_{\nu}^{\text{SSH}} = \pi(1/a, 1/b)$, indicating a non-trivial response for *any* \mathcal{I} -symmetric pair of dislocations with a Burgers vector \mathbf{B} that is an odd combination of lattice basis vectors. We introduce pairs of \mathcal{I} -symmetric dislocations with $\mathbf{B} = \mathbf{a}_2 = (0, b)$ for BP, satisfying Eq. (3). As summarized in Fig. 1, we observe a non-trivial dislocation response, manifested at $\lambda = 0$ in the presence of two exactly overlapping bound states which lie in the middle of the energy gap. Their degeneracy arises from the fact that they are related by \mathcal{I} symmetry and that the defects are located far away from each other. We plot the full spectrum against λ [Fig. 1(c)] to see where the bound states end up in the realistic model. As $\lambda \rightarrow 1$, polarization states merge with the valence band; however they still create a state counting imbalance between conduction and valence bands that implies a filling anomaly [53] at $5/8$ filling. As a measure of localization, we compute the site-resolved inverse participation ratio (IPR), defined as

$$\text{IPR} = \sum_i \left(\sum_n |\psi_{i,n}|^2 \right)^2 \quad (8)$$

where $\psi_{i,n}$ denotes the wavefunction component of orbital n at lattice site i . We show the result in Fig. 1(c). The localization length of the dislocation bound states scales inversely with the energy gap as expected [58, 64]. We plot the corresponding real-space density profile in Figs. 1(e) and (f).

Dislocation response of 3D semiconductors— We next discuss silicon, diamond, and germanium, with spatial geometry depicted in Fig. 2(d) and lattice constants $a = 2.698, 1.798$ and 2.829 Å, respectively. For all three materials, we consider well-known tight-binding Hamiltonians with parameters from Ref. 65 (see also Ref. 66). In the BZ, the Bloch Hamiltonian restricted to the 1D lines connecting points X_i to L for $i = 1, 2, 3$, with inversion eigenvalues shown in Figs. 2(a) and (b), all feature an odd number of band inversions with respect to the reference atomic limit [67]. For all three semiconductors, Eq. (5) then gives $(\nu_{2,3}^{\text{SSH}}, \nu_{3,1}^{\text{SSH}}, \nu_{2,1}^{\text{SSH}}) = (1, 1, 1)$, as calculated in the Supplemental Material (SM) [67]. These invariants imply that Eq. (6) is satisfied for *any* pair of *edge* dislocations when \mathbf{B} and \mathbf{T} are lattice basis vectors. We introduce pairs of \mathcal{I} -symmetric dislocations with $\mathbf{B} = \mathbf{a}_1 = a/2(0, 1, 1)$ and $\mathbf{T} = \mathbf{a}_3 = a/2(1, 1, 0)$, satisfying Eq. (6) and find that mid-gap dislocation bands are present even at realistic model parameters. We summarize our results in Fig. 2 for silicon, and relegate similar plots for diamond and germanium to the SM. As in Fig. 1, we use the IPR to study the localization properties of the dislocation bound states. The IPR is smallest at $\kappa_3 = \mathbf{k} \cdot \mathbf{a}_3/2\pi = 0$ and largest at $\kappa_3 = 1/2$. We show the real-space density profile of the dislocation states in Figs. 2(e) and (f). At half-filling, there is a filling anomaly *per momentum* κ_3 [9].

Discussion— Using well-known tight-binding models, we have shown that several elementary semiconductors can host dislocation bound states. In 3D, this response can be non-trivial for edge dislocations but is always trivial for screw dislocations. These polarization states have a topologically robust filling anomaly, as diagnosed by 2D and 3D weak SSH invariants $\mathbf{M}_{\nu}^{\text{SSH}}$ [9] and $\hat{M}_{\nu}^{\text{SSH}}$. As long as the polarization states remain close to the Fermi energy, they could be probed experimentally using e.g. scanning tunneling microscopy, as was already done in bismuth for screw dislocations [22]. A clear next step would be to extend our theory beyond \mathcal{I} -symmetry to materials with other crystalline symmetries.

Acknowledgments— We thank Malcolm Connolly for early discussions on this idea. F.S. thanks Benjamin Wieder, Andrei Bernevig and Titus Neupert for a previous collaboration on a similar topic. A.C. acknowledges support from Imperial College London via a President's PhD Scholarship. This work was supported by a UKRI Future Leaders Fellowship MR/Y017331/1.

-
- [1] X.-G. Wen, Colloquium: Zoo of quantum-topological phases of matter, *Rev. Mod. Phys.* **89**, 041004 (2017).
- [2] M. Z. Hasan and C. L. Kane, Colloquium: Topological insulators, *Rev. Mod. Phys.* **82**, 3045 (2010).
- [3] M. G. Vergniory, L. Elcoro, C. Felser, N. Regnault, B. A. Bernevig, and Z. Wang, A complete catalogue of high-quality topological materials, *Nature* **566**, 480–485 (2019).
- [4] K. W. Böer and U. W. Pohl, Crystal defects, in *Semiconductor Physics* (Springer International Publishing, Cham, 2023) pp. 595–648.
- [5] Y. Ran, Y. Zhang, and A. Vishwanath, One-dimensional topologically protected modes in topological insulators with lattice dislocations, *Nature Physics* **5**, 298 (2009).
- [6] J. C. Y. Teo and C. L. Kane, Topological defects and gapless modes in insulators and superconductors, *Phys. Rev. B* **82**, 115120 (2010).
- [7] V. Juričić, A. Mesaros, R.-J. Slager, and J. Zaanen, Universal probes of two-dimensional topological insulators: Dislocation and π flux, *Phys. Rev. Lett.* **108**, 106403 (2012).
- [8] R. Queiroz, I. C. Fulga, N. Avraham, H. Beidenkopf, and J. Cano, Partial lattice defects in higher-order topological insulators, *Phys. Rev. Lett.* **123**, 266802 (2019).
- [9] F. Schindler, S. S. Tsirkin, T. Neupert, B. Andrei Bernevig, and B. J. Wieder, Topological zero-dimensional defect and flux states in three-dimensional insulators, *Nature Communications* **13**, 10.1038/s41467-022-33471-x (2022).
- [10] S. S. Yamada, T. Li, M. Lin, C. W. Peterson, T. L. Hughes, and G. Bahl, Bound states at partial dislocation defects in multipole higher-order topological insulators, *Nature Communications* **13**, 2035 (2022).
- [11] D. Zhu, D. Liu, Z.-Y. Zhuang, Z. Wu, and Z. Yan, Field-sensitive dislocation bound states in two-dimensional d -wave altermagnets, *Phys. Rev. B* **110**, 165141 (2024).
- [12] J. Paulose, B. G.-g. Chen, and V. Vitelli, Topological modes bound to dislocations in mechanical metamaterials, *Nature Physics* **11**, 153 (2015).
- [13] F.-F. Li, H.-X. Wang, Z. Xiong, Q. Lou, P. Chen, R.-X. Wu, Y. Poo, J.-H. Jiang, and S. John, Topological light-trapping on a dislocation, *Nature Communications* **9**, 2462 (2018).
- [14] I. H. Grinberg, M. Lin, W. A. Benalcazar, T. L. Hughes, and G. Bahl, Trapped state at a dislocation in a weak magnetomechanical topological insulator, *Phys. Rev. Appl.* **14**, 064042 (2020).
- [15] J.-X. Zhong, B. Roy, and Y. Jing, Observation of dislocation bound states and skin effects in non-hermitian chern insulators, *Advanced Materials* **n/a**, e15496 (2026).
- [16] H. Xue, D. Jia, Y. Ge, Y.-j. Guan, Q. Wang, S.-q. Yuan, H.-x. Sun, Y. D. Chong, and B. Zhang, Observation of dislocation-induced topological modes in a three-dimensional acoustic topological insulator, *Phys. Rev. Lett.* **127**, 214301 (2021).
- [17] R.-J. Slager, A. Mesaros, V. Juričić, and J. Zaanen, Interplay between electronic topology and crystal symmetry: Dislocation-line modes in topological band insulators, *Phys. Rev. B* **90**, 241403 (2014).
- [18] B. Roy and V. Juričić, Dislocation as a bulk probe of higher-order topological insulators, *Phys. Rev. Res.* **3**, 033107 (2021).
- [19] Y. Liu, X. Zhang, C.-P. Liang, F.-F. Li, Y. Poo, and J.-H. Jiang, Observation of bulk-dislocation correspondence in photonic crystals, *Phys. Rev. Appl.* **22**, 064097 (2024).
- [20] F. Schindler and A. Prem, Dislocation non-hermitian skin effect, *Phys. Rev. B* **104**, L161106 (2021).
- [21] L.-H. Hu and R.-X. Zhang, Dislocation majorana bound states in iron-based superconductors, *Nature Communications* **15**, 2337 (2024).
- [22] A. K. Nayak, J. Reiner, R. Queiroz, F. Huixia, and H. Beidenkopf, Resolving the topological classification of bismuth with topological defects, *Science Advances* **5**, eaax6996 (2019), pMID: 31701006, PMCID: PMC6824853.
- [23] Z.-K. Lin, Q. Wang, Y. Liu, H. Xue, B. Zhang, Y. Chong, and J.-H. Jiang, Topological phenomena at defects in acoustic, photonic and solid-state lattices, *Nature Reviews Physics* **6**, 149 (2024), published online 10 July 2023; Author Correction published 5 December 2023.
- [24] L. Ye, C. Qiu, M. Xiao, T. Li, J. Du, M. Ke, and Z. Liu, Topological dislocation modes in three-dimensional acoustic topological insulators, *Nature Communications* **13**, 10.1038/s41467-022-28182-2 (2022), published online 26 January 2022.
- [25] Others include: α -Sn, with near-zero band gap and potential band inversions induced by strain at the Γ point, which does not contribute to a dislocation response; and boron, whose tight-binding model has a complex structure and large unit cell, rendering the study of dislocation-bound states significantly more involved.
- [26] B. Bradlyn, L. Elcoro, J. Cano, M. G. Vergniory, Z. Wang, C. Felser, M. I. Aroyo, and B. A. Bernevig, Topological quantum chemistry, *Nature* **547**, 298–305 (2017).
- [27] Z. Liu, P. Deng, Y. Xu, H. Yang, D. Pei, C. Chen, S. He, D. Liu, S.-K. Mo, T. Kim, C. Cacho, H. Yao, Z.-D. Song, X. Chen, Z. Wang, B. Yan, L. Yang, B. A. Bernevig, and Y. Chen, Massive 1d dirac line, solitons and reversible manipulation on the surface of a prototype obstructed atomic insulator, silicon (2024), arXiv:2406.08114 [cond-mat.mes-hall].
- [28] X.-P. Li, D.-S. Ma, C.-C. Liu, Z.-M. Yu, and Y. Yao, From atomic semimetal to topological nontrivial insulator, *Phys. Rev. B* **105**, 165135 (2022).
- [29] L. Elcoro, B. J. Wieder, Z. Song, Y. Xu, B. Bradlyn, and B. A. Bernevig, Magnetic topological quantum chemistry, *Nature Communications* **12**, 10.1038/s41467-021-26241-8 (2021).
- [30] D.-S. Ma, K. Yu, X.-P. Li, X. Zhou, and R. Wang, Obstructed atomic insulators with robust corner modes, *Phys. Rev. B* **108**, L100101 (2023).
- [31] Y. Xu, L. Elcoro, Z.-D. Song, M. G. Vergniory, C. Felser, S. S. P. Parkin, N. Regnault, J. L. Mañes, and B. A. Bernevig, Filling-enforced obstructed atomic insulators, *Phys. Rev. B* **109**, 165139 (2024).
- [32] L. Wang, Y. Jiang, J. Liu, S. Zhang, J. Li, P. Liu, Y. Sun, H. Weng, and X.-Q. Chen, Two-dimensional obstructed atomic insulators with fractional corner charge in the MA_2Z_4 family, *Phys. Rev. B* **106**, 155144 (2022).
- [33] Y. Xu, L. Elcoro, G. Li, Z.-D. Song, N. Regnault, Q. Yang, Y. Sun, S. Parkin, C. Felser, and B. A. Bernevig, Three-dimensional real space invariants, obstructed atomic insulators and a new principle for active catalytic sites (2021), arXiv:2111.02433 [cond-mat.mtrl-]

- sci].
- [34] F. Schindler and B. A. Bernevig, Noncompact atomic insulators, *Phys. Rev. B* **104**, L201114 (2021).
- [35] X. Ding, X. Jin, Z. Chen, X. Lv, D.-S. Ma, X. Wu, and R. Wang, Abundant surface-semimetal phases in three-dimensional obstructed atomic insulators, *Phys. Rev. B* **108**, 085135 (2023).
- [36] X.-R. Liu, M.-Y. Zhu, Y. Feng, M. Zeng, X.-M. Ma, Y.-J. Hao, Y. Dai, R.-H. Luo, Y.-P. Zhu, K. Yamagami, Y. Liu, S. Cui, Z. Sun, J.-Y. Liu, Y. Huang, Z. Liu, M. Ye, D. Shen, B. Li, and C. Liu, Observation of floating surface state in obstructed atomic insulator candidate nip2, *npj Quantum Materials* **9**, 85 (2024).
- [37] J. Cano, L. Elcoro, M. I. Aroyo, B. A. Bernevig, and B. Bradlyn, Topology invisible to eigenvalues in obstructed atomic insulators, *Phys. Rev. B* **105**, 125115 (2022).
- [38] Y. Li, J. Wang, S. Qian, W. Meng, and X. Wang, Obstructed atomic insulator inorganic electrides, *Phys. Rev. B* **112**, 205112 (2025).
- [39] O. Arroyo-Gascón, S. Bravo, M. Pacheco, and L. Chico, Two-dimensional orbital-obstructed insulators with higher-order band topology, *Phys. Rev. B* **112**, 075114 (2025).
- [40] I. A. Day, A. Varentcova, D. Varjas, and A. R. Akhmerov, Pfaffian invariant identifies magnetic obstructed atomic insulators, *SciPost Phys.* **15**, 114 (2023).
- [41] J. Wang, T.-T. Zhang, Q. Zhang, X. Cheng, W. Wang, S. Qian, Z. Cheng, G. Zhang, and X. Wang, 3d carbon allotropes: Topological quantum materials with obstructed atomic insulating phases, multiple bulk-boundary correspondences, and real topology, *Advanced Functional Materials* **34**, 2316079 (2024).
- [42] S. K. Radha and W. R. L. Lambrecht, Topological obstructed atomic limit insulators by annihilating dirac fermions, *Phys. Rev. B* **103**, 075435 (2021).
- [43] R. Verma, S.-M. Huang, and B. Singh, Atomically thin obstructed atomic insulators with robust edge modes and quantized spin hall effect, *Phys. Rev. B* **110**, 165122 (2024).
- [44] Q. Marsal, D. Varjas, and A. G. Grushin, Obstructed insulators and flat bands in topological phase-change materials, *Phys. Rev. B* **107**, 045119 (2023).
- [45] G. Singh, S. Bera, and V. B. Shenoy, Arboreal obstructed atomic insulating and metallic phases of fermions, *Phys. Rev. B* **110**, 205143 (2024).
- [46] V. Nuñez, S. Bravo, J. D. Correa, L. Chico, and M. Pacheco, Higher-order obstructed atomic insulator phase in pentagonal monolayer pdse2, *2D Materials* **11**, 015015 (2023).
- [47] H. Wada and S. Murakami, Local expression of fractional corner charges in obstructed atomic insulators and relationship with the fractional disclination charges, *Phys. Rev. B* **113**, 075306 (2026).
- [48] Y. Hwang, V. Gupta, F. Schindler, L. Elcoro, Z. Song, B. A. Bernevig, and B. Bradlyn, Stable real-space invariants and topology beyond symmetry indicators (2025), arXiv:2505.09697 [cond-mat.mes-hall].
- [49] J. Herzog-Arbeitman, V. Peri, F. Schindler, S. D. Huber, and B. A. Bernevig, Superfluid weight bounds from symmetry and quantum geometry in flat bands, *Phys. Rev. Lett.* **128**, 087002 (2022).
- [50] G. H. Wannier, The structure of electronic excitation levels in insulating crystals, *Phys. Rev.* **52**, 191 (1937).
- [51] W. P. Su, J. R. Schrieffer, and A. J. Heeger, Solitons in polyacetylene, *Phys. Rev. Lett.* **42**, 1698 (1979).
- [52] W. P. Su, J. R. Schrieffer, and A. J. Heeger, Soliton excitations in polyacetylene, *Phys. Rev. B* **22**, 2099 (1980).
- [53] W. A. Benalcazar, T. Li, and T. L. Hughes, Quantization of fractional corner charge in C_n -symmetric higher-order topological crystalline insulators, *Phys. Rev. B* **99**, 245151 (2019).
- [54] F. Schindler, M. Brzezińska, W. A. Benalcazar, M. Iraola, A. Bouhon, S. S. Tsirkin, M. G. Vergniory, and T. Neupert, Fractional corner charges in spin-orbit coupled crystals, *Phys. Rev. Res.* **1**, 033074 (2019).
- [55] L. Fu, C. L. Kane, and E. J. Mele, Topological insulators in three dimensions, *Phys. Rev. Lett.* **98**, 106803 (2007).
- [56] L. Fu and C. L. Kane, Topological insulators with inversion symmetry, *Phys. Rev. B* **76**, 045302 (2007).
- [57] Y. Takao, H. Asahina, and A. Morita, Electronic structure of black phosphorus in tight binding approach, *Journal of the Physical Society of Japan* **50**, 3362 (1981).
- [58] R. D. King-Smith and D. Vanderbilt, Theory of polarization of crystalline solids, *Phys. Rev. B* **47**, 1651 (1993).
- [59] D. Vanderbilt and R. D. King-Smith, Electric polarization as a bulk quantity and its relation to surface charge, *Phys. Rev. B* **48**, 4442 (1993).
- [60] A. Alexandradinata, X. Dai, and B. A. Bernevig, Wilson-loop characterization of inversion-symmetric topological insulators, *Phys. Rev. B* **89**, 155114 (2014).
- [61] K.-I. Imura, Y. Takane, and A. Tanaka, Weak topological insulator with protected gapless helical states, *Phys. Rev. B* **84**, 035443 (2011).
- [62] M. Hitomi, T. Kawakami, and M. Koshino, Multiorbital edge and corner states in black phosphorene, *Phys. Rev. B* **104**, 125302 (2021).
- [63] See the Supplemental Material for calculations of invariants, as well as a plot summarizing results for diamond and germanium.
- [64] R. Resta, Macroscopic polarization in crystalline dielectrics: the geometric phase approach, *Rev. Mod. Phys.* **66**, 899 (1994).
- [65] M. Nakhaee, S. A. Ketabi, and F. M. Peeters, Tight-binding studio: A technical software package to find the parameters of tight-binding hamiltonian, *Computer Physics Communications* **254**, 107379 (2020).
- [66] J. C. Slater and G. F. Koster, Simplified lcao method for the periodic potential problem, *Phys. Rev.* **94**, 1498 (1954).
- [67] For all materials, we choose \mathcal{I} -symmetric unit cells, implying vanishing polarization in the reference atomic limit.

Supplemental Material for “Topological Dislocation Response in Elementary Semiconductors”

Yuteng Zhou,¹ Alexandre Chaduteau,¹ and Frank Schindler¹

¹*Blackett Laboratory, Imperial College London, London SW7 2AZ, United Kingdom*

I. NUMERICAL RESULTS: DIAMOND AND GERMANIUM

We summarize the numerical results for diamond and germanium in Fig. 1. In addition we calculate the weak SSH invariants for black phosphorene (BP) and silicon (and hence also diamond and germanium) here.

For BP, using the inversion eigenvalues in Figs. 1(a) and (b) and Eq. (2) in the main text, we obtain

$$\begin{aligned}\nu_1^{\text{SSH}} &= \frac{1}{2}(1 - \delta_{M=(1,1)}\delta_{X=(1,0)}) = 1, \\ \nu_2^{\text{SSH}} &= \frac{1}{2}(1 - \delta_{M=(1,1)}\delta_{Y=(0,1)}) = 1.\end{aligned}\tag{1}$$

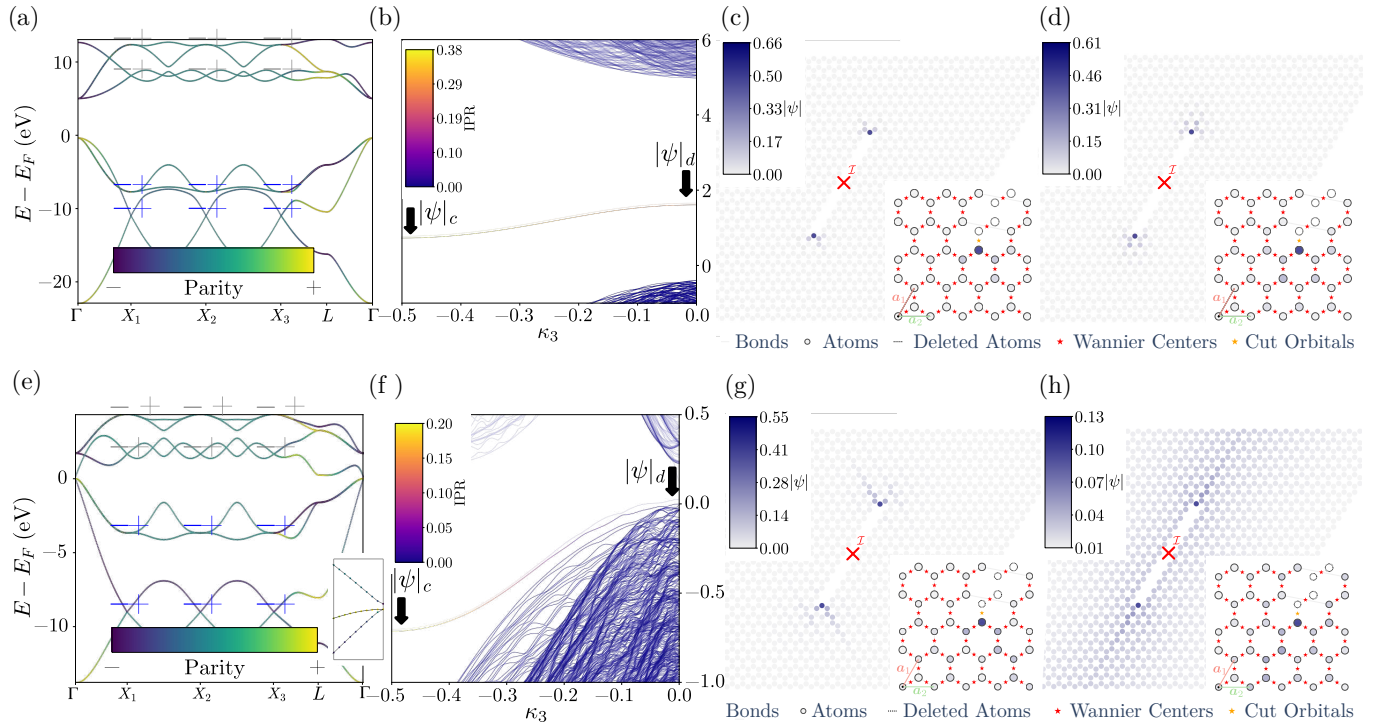


FIG. 1. Tight-binding simulations of 3D diamond and germanium. (a) Energy dispersion relation for diamond, when following the path shown in the main text’s Fig. 2(a), with associated inversion parity eigenvalues at TRIM points. (b) Corresponding diamond band structure, with energies plotted against the only translationally-invariant direction κ_3 , which is along \mathbf{b}_3 . (c) and (d) Corresponding real-space wavefunction $|\psi|$ plots for polarization states at $\kappa_3 = -1/2$ and $\kappa_3 = 0$, respectively. (e) Energy dispersion relation for germanium, when following the same path as in (a). (f) Corresponding germanium band structure, as in (b) for diamond. (g) and (h) Germanium real-space wavefunction plots similar to (c) and (d). In (a) and (e), blue-colored eigenvalues are for occupied bands; gray-colored eigenvalues are for unoccupied bands. Two inversion-related polarization bands appear in the middle of the gap for both (b) and (f). Although in each case we shifted one of them slightly for visualization, these two bands overlap when the gap is large. We color-code the IPR for these bands. It is maximal at $\kappa_3 = -\frac{1}{2}$ and minimal at $\kappa_3 = 0$, see (c) and (d), and (g) and (h).

On the other hand, using the inversion eigenvalues in Figs. 2(a) and (b) and Eq. (5) in the main text, we have

$$\begin{aligned}
 \nu_{2,3}^{\text{SSH}} = \nu_{3,2}^{\text{SSH}} &= \frac{1}{2} [1 - \delta_{X_1=(0,1,1)} \delta_{L=(1,1,1)}] = 1, \\
 \nu_{3,1}^{\text{SSH}} = \nu_{1,3}^{\text{SSH}} &= \frac{1}{2} [1 - \delta_{X_2=(1,0,1)} \delta_{L=(1,1,1)}] = 1, \\
 \nu_{2,1}^{\text{SSH}} = \nu_{1,2}^{\text{SSH}} &= \frac{1}{2} [1 - \delta_{X_3=(1,1,0)} \delta_{L=(1,1,1)}] = 1
 \end{aligned} \tag{2}$$

for all three 3D semiconductors silicon, diamond, and germanium.